Refractive components for magnetic atom optics

W. G. Kaenders, F. Lison,* I. Müller, A. Richter, R. Wynands,* and D. Meschede*
Institut für Quantenoptik, Universität Hannover, Welfengarten 1, D-30167 Hannover, Germany
(Received 1 May 1996)

With strong rare-earth permanent magnets we have built highly refractive atom-optical components for laser-cooled atoms. We have studied the influence of axially symmetric multipole components on a cesium atomic beam. In analogy to traditional optics the action of a quadrupole ring parallels a conical prism, or axicon. Hexapole lenses were applied for focusing with a more than 1000-fold increase in atomic flux density at the focal spot and for imaging with the atomic beam. Two hexapole lenses were combined to form a telescope, which was operated off axis in order to separate fast thermal and slowed atoms. The experiments can approximately be described in terms of geometrical optics. [S1050-2947(96)07812-2]

PACS number(s): 03.75.Be, 42.50.Vk

I. INTRODUCTION

It is the purpose of this work to redraw attention to the classical method of neutral atom optics relying on the deflection of paramagnetic atoms by inhomogeneous magnetic fields. The close analogy between atomic and optical rays in terms of traditional optics was realized when hexapole lenses were invented [1], but can already be traced back to the famous early atomic beam experiments by Stern [2] in the 1920s and their successor, the Rabi apparatus [3].

In recent years the field of neutral atom optics has been revived by the application of light forces. Mechanical action on atomic beams can be exerted through dissipative radiation pressure or through conservative dipole forces derived from near-resonant or intense laser beams [4]. Many components of classical ray optics such as prisms, beam splitters, mirrors, and lenses have been demonstrated experimentally with laser light. Diffraction of matter waves by standing light wave gratings is very conveniently applied in atomic interferometry [5,6]. However, the usefulness of these laser light components for conventional applications is often limited by the small aperture that can be achieved.

Although electromagnetic lenses with hexapole and quadrupole symmetry had been realized in the early 1950s [1], applications have remained scarce. Notable exceptions include atomic clocks and hydrogen masers in which hexapole lenses serve to increase atomic flux densities as well as to magnetically polarize a thermal beam [7].

The main obstacle for magnetic atom optics has been the low refractive power of magnetic components at conventional laboratory field intensities, which for atoms effusing from a heated oven have unpractically large focal lengths of much more than 1 m. Furthermore, the optical quality is seriously afflicted by the broad velocity distribution in such a thermal beam through the strong variation of the focal length f with atomic velocity v ($f \propto v^2$). Supersonic beams can reduce the velocity spread $\Delta v/v$ but generate an even higher average atomic beam velocity resulting in smaller refractive power.

In recent years laser cooling of a thermal atomic beam has made efficient reduction of both the atomic velocity (e.g., the focal length) and the velocity spread possible. Focusing of a laser-cooled atomic beam by an electromagnetic lens was first reported by Metcalf, Philips, and Prodan [8], and an increase in flux density by a factor of 10 was achieved.

We have used a laser-prepared slow atomic cesium beam with a narrow velocity distribution for a systematic investigation of the action of axial magnetic quadrupoles and hexapoles on the atomic beam propagation. In combination with components manufactured from strong permanent magnetic materials the refractive power was increased enough to realize convenient focal lengths of a few cm. While in this work we report on transmissive magnetic components in analogy to optical lenses it is possible to also establish a reflective version of magnetic atom optics [9,10]. The first magnetic mirror was demonstrated by Hinds and co-workers [11].

With inhomogeneous magnetic fields it is possible to deflect beams of paramagnetic atoms. Such atoms are generally found in uneven groups of the periodic system of elements, for instance, the alkali metals. The energy of a magnetic dipole in a magnetic field with flux density $\mathbf{B}$ is known from classical electrodynamics,

$$V_{\mathrm{dip}} = -\boldsymbol{\mu}\cdot\mathbf{B} \tag{1}$$

and the corresponding force is

$$\mathbf{F}_{\mathrm{mag}} = \nabla(\boldsymbol{\mu}\cdot\mathbf{B}) = (\boldsymbol{\mu}\cdot\nabla)\mathbf{B} \tag{2}$$

for a constant magnetic moment $\boldsymbol{\mu}$. Since polarized atomic beams are most interesting for neutral atom optics—and can be prepared by optical pumping—the discussion can be restricted to atoms with magnetic moment $\boldsymbol{\mu}$ either parallel or antiparallel to the direction of the magnetic flux density $\mathbf{B}$. Atoms forced towards stronger (weaker) flux density are called high-field-seeking (low-field-seeking) atoms. It is tolerable to neglect the contribution of the nuclear moment. The total magnetic moment is then $\mu = \mu_B$ for $J = \frac{1}{2}$ states, for instance, in alkali atoms, or $\mu = 2\mu_B$ for $J = \frac{3}{2}$ atoms, for instance, Al, Ga, or In. For a field gradient of 1 T/cm fully

*Present address: Institut für Angewandte Physik, Rheinische Friedrich-Wilhelms-Universität Bonn, Wegelerstrasse 8, D-53115 Bonn, Germany.

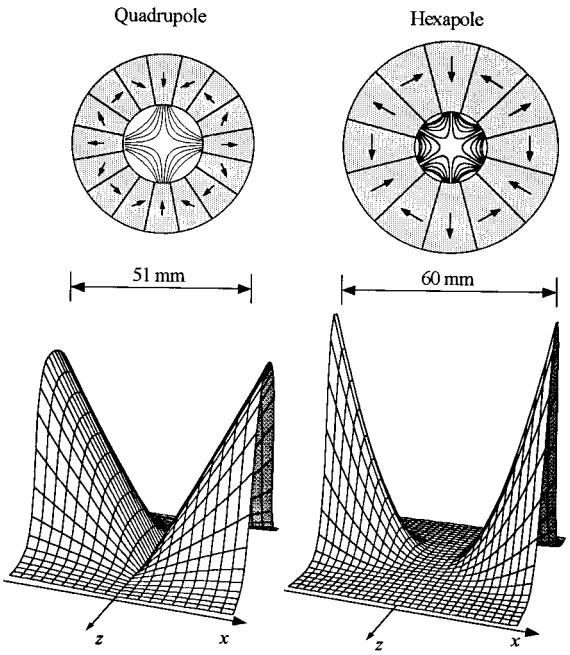

FIG. 1. Configurations of permanent magnets that form a plane magnetic quadrupole ($2n=4$) and a magnetic hexapole ($2n=6$) with flux lines sketched in the inner bore. Shown in the bottom part are equipotential surfaces for low-field-seeking paramagnetic atoms in the corresponding magnetic rings of finite length.

aligned hydrogen atoms experience an acceleration $F_{\max}/m_H=5\times10^4 g$, whereas the heavier cesium atoms undergo $400g$ acceleration.

Large magnetic flux densities are essential for the construction of highly refractive magnetic components. The current densities required to generate such large field inhomogeneities from solenoids are large and an ambitious task even with superconducting coils. Rare-earth magnetic materials (REM's), however, with both large magnetic remanence B_r and high coercive field strength H_c are particularly useful and readily available to construct magnetic components with very strong gradients for neutral atom optics.

II. CONSTRUCTION OF PERMANENT MAGNETIC COMPONENTS

A. Concepts

The concept of plane magnetic multipoles constructed from REM's was pioneered by Halbach [12] for applications in charged-particle accelerators. The relative susceptibility of REM's such as SmCo or Nd-Fe-B is very close to unity and the magnetization is constant over a wide range of external magnetic field strengths. Therefore the total magnetic field of an arrangement consisting of more than one REM piece can be determined from the superposition principle if the use of high flux materials is avoided (*iron-free structures*), allowing the application of elegant methods of potential theory, such as conformal mapping. In practice the field distribution can be predicted at the 1% level once the geometry of the individual REM segments is known [13].

Transmissive magnetic components useful for atom optics have cylindrical geometry as shown in Fig. 1. The amplitude of the magnetization $\mathbf{M}$ is constant, $|\mathbf{M}|=M_0=B_r/\mu_0$, while the direction of $\mathbf{M}$ varies to obtain the desired multipole symmetry. The magnetic potential Φ_M can then be given in terms of a Fourier sum, and a pure magnetic $2n$ pole, where n is called the order of the multipole, is expected if just a single Fourier component of the magnetization is present:

$$M_\rho(n)=M_0\cos n\phi,$$
$$M_\phi(n)=M_0\sin n\phi, \tag{3}$$

In this case the potential in the inner bore of a cylindrical element with magnetization according to Eq. (3) and inner and outer radius ρ_1 and ρ_2, respectively, is given in cylindrical coordinates (ρ,ϕ) by

$$\Phi_M(n)=B_r K_n(\rho_1,\rho_2)\rho_1(\rho/\rho_1)^n\cos n\phi, \tag{4}$$

where the expansion coefficient reads

$$K_n(\rho_1,\rho_2)=[1-(\rho_1/\rho_2)^n]/(n-1). \tag{5}$$

The flux density distribution is then calculated from

$$\mathbf{B}=\nabla\Phi_M. \tag{6}$$

The most important cases for neutral atom optics are the *quadrupole* field for $2n=4$ and the *hexapole* field for $2n=6$. Interestingly the field outside the cylindrical structure ($\rho>\rho_2$) completely vanishes and is very small in real components, which is convenient or even essential for most applications.

In practice the magnetization does not vary continuously with angle ϕ but is approximated with discrete, homogeneously magnetized segments, as indicated in Fig. 1. The segmentation causes a weakening of the desired multipole strength and also gives rise to unwanted higher-order multipoles. Halbach has introduced a geometry factor $G_{S,n}$ accounting for the piecewise rotation of the magnetization. For a multipole of order n constructed from S homogeneously magnetized and pie-shaped segments it is

$$G_{S,n}=\frac{\sin(n+1)\pi/S}{(n+1)\pi/S}<1. \tag{7}$$

Higher multipoles of order n' enter for

$$n'=n+\nu S,$$
$$\nu=1,2,\ldots \tag{8}$$

and are usually insignificant in the center of the aperture of the magnetic component.

For neutral atom optics the most important quantity in any multipole component is the variation of the magnitude of the flux density, which in a perfect multipole only depends on the distance ρ from the geometric axis,

$$|\mathbf{B}(\rho,\phi)|=B_n(\rho/\rho_1)^{n-1}, \tag{9}$$

where B_n is the strength of the flux density at the outer edge of the aperture, which is

TABLE I. Properties of the three different magnetic components used in the experiments.

	Quadrupole	Hexapole type I	Hexapole type II
Multipole order n	2	3	3
Material	$SmCo_5$	Nd-Fe-B	Nd-Fe-B
Permeability μ_r	1.02	1.08	1.08
Remanence B_r (T)	0.95	1.12	1.12
Number of segments S	16	12	12
Geometry factor $G_{S,n}$	0.94	0.83	0.83
Inner radius ρ_1 (mm)	11	7.5	15
Outer radius ρ_2 (mm)	25.5	30	30
Length L (mm)	38.1	25	20
$B(\rho_1)$ (T)	0.96	1.3	0.83
$\partial B/\partial\rho$ (T/cm)	0.87		
$\partial^2 B/\partial\rho^2$ (T/cm^2)		2.3	0.37
$[1-(\rho_1/\rho_2)^n]G_{S,n}$	0.76	0.82	0.73

$$B_2 = 2B_r[1-(\rho_1/\rho_2)^2]G_{S,2}, \qquad B_3 = \tfrac{3}{2}B_r[1-(\rho_1/\rho_2)^3]G_{S,3} \tag{10}$$

for quadrupole and hexapole. In Table I we have collected essential data for these components showing that with moderate effort about 80% of the perfect multipole strength ($\rho_1/\rho_2 \to 0, G_{S,n} \to 1$) can be realized.

While Eqs. (3)–(7) are valid for infinitely long multipoles, the influence of the finite length L needs to be considered for more delicate optical applications, e.g., imaging or focusing. The fringe fields retain the symmetry properties of the plane multipole, and Halbach [12] has also given prescriptions for an analytical treatment. Following that prescription we obtained a series expansion for the magnetic flux density of our finite multipoles. The final expression is long and complicated, and here we present only a summary of the main results. The calculated radial potential experienced by a low-field-seeking atom is shown in Fig. 1 whereas Fig. 2 shows a cross section of the calculated and measured magnetic flux density across the center of a hexapole ring. For the calculation only the first two terms of the series expansion were retained. Near the center the agreement is very good while at larger radii the truncation of the series leads to small deviations. A closer look at those deviations shows that they have the same radial dependence as the first neglected term in the series expansion. In order to achieve the magnetic flux density of the corresponding infinite multipole in the center of the component the length L of the magnetic component has to be at least twice the inner radius ρ_1 [12]. The analytic description of the finite multipole rings is useful in a theoretical investigation of the optical aberrations, for instance; this will be discussed in a separate publication.

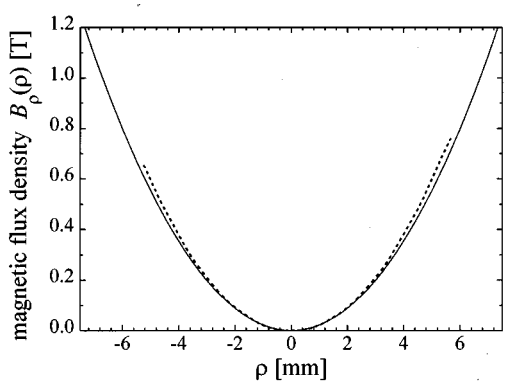

FIG. 2. Calculated (solid line) and measured (dashed line) magnetic flux density across the center of a hexapole ring type I (cf. Table I) with $L=25$ mm, $\rho_1=7.5$ mm, and $\rho_2=30$ mm.

B. Manufacturing and controlling

For fabrication of the magnetic components the highly anisotropic, unmagnetized raw material was bought as sintered blocks with typical dimensions $50\times50\times100$ mm^3. The direction of the easy axis in each block is misaligned with respect to the block axes by up to 3° as a result of the production process. Only the inner 75% of the volume were used in order to reduce the influence of manufacturing tolerances. Wire erosion was used to cut segments of about 1 cm^3 each. The segments were then magnetized and assembled in aluminum ring holders. For improved performance it is possible to align individual elements in an effort to tune away undesired multipoles, and also to select segments for optimum contribution by measuring each individual magnetic moment with a fluxmeter.

The dominant multipole contribution of our fully assembled magnetic components was examined by means of a Hall probe. In Fig. 2 the result of such a measurement is compared with the calculated values.

The investigation of higher-order multipole components requires diagnostics of rapidly varying distributions of magnetic flux density with spatial resolution at the 100-μm level or below. The widths of standard Hall probes (2 mm in our case) are insufficient for this purpose. Instead, the axial symmetry suggests rotation of an induction coil inside the multipole magnet, or the rotation of the multipole magnet around the coil. Fourier components of the induced voltage are proportional to the strength of the corresponding multipole. In order to achieve a maximum sensitivity it is necessary to nearly fill out the complete inner bore of the magnetic multipole with the coil [14,15]. High accuracy, however, is very difficult to achieve in practice because of the extreme sensi-

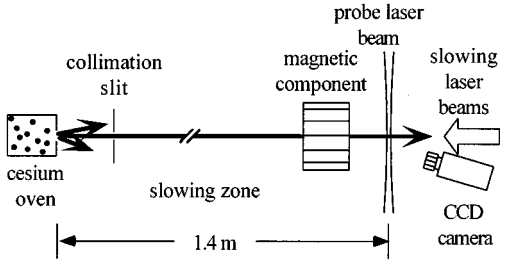

FIG. 3. The experimental setup, showing the atomic oven, a slit with a mechanical shutter, the atomic beam, the slowing and repumping lasers, and the detection zone. The magnetic components are introduced into the atomic-beam path as marked and their action on the optically prepared atomic-beam is recorded with a CCD camera by atomic fluorescence detection with a light sheet technique [19].

tivity to coil misalignment and variations in angular velocity.

A third method to map the magnetic flux density of the multipole rings employs fluorescence from an atomic beam and will be described in Sec. IV A.

III. EXPERIMENTAL SETUP

A. Estimate of refractive power

We assume a typical magnetic flux density gradient of $\beta = dB/dz = 1$ T/cm at the aperture $D = 2\rho_1 \approx 1$ cm of a magnetic component of length L. With longitudinal atomic velocity $v^2 = 2E_{\rm kin}/m$ and $v_\perp = \mu_B \beta L/(vm)$ the small deflection angle caused by this component is $\alpha = v_\perp / v$ from which one calculates an effective focal length

$$f = DE_{\rm kin}/\mu_B \beta L. \tag{11}$$

At thermal kinetic energies equivalent to 410 K Eq. (11) yields $f \approx 600$ cm/(L/cm). Therefore laser cooling is an essential experimental requirement to obtain convenient focal lengths in the 5–10-cm domain for components with typical lengths of 2 cm.

B. The slow atomic beam

A cesium atomic beam is slowed by the chirp cooling method [16,17]. The thermal atomic beam ($T = 410$ K, $v_{\rm rms} = 300$ m/s) from a resistively heated oven with a nozzle diameter of 1 mm is collimated by an aperture (1 mm diameter) to a ratio of 1/330 (Fig. 3). 852-nm light is derived from two diode lasers to cycle the $F = 4 \rightarrow 5$ transition of the D_2 line and to recover atoms pumped to the uncycled $F = 3$ ground state. Laser frequencies are chirped to maintain resonance with the decelerating atoms. Both beams are circularly polarized and focused into the vacuum chamber and into the oven aperture, so that they completely overlap the atomic beam. Their power densities are sufficient to saturate the $4 \rightarrow 5$ transition ($I_{\rm sat} = 2.2$ mW/cm^2) and fulfill the repumping condition ($I_{\rm repump} > 50$ μW/cm^2) everywhere along the atomic beam path. A small longitudinal magnetic flux density of 5 G generated by a solenoid along the slowing section preserves the orientation of the magnetic moments. A mechanical chopper in the light path with a rise time of $t < 50$ μs determines the 10-Hz cooling cycle. For 7 ms the lasers are chirped with a rate of typically 50 MHz/ms. The light is then blocked by the chopper blade for 93 ms while the lasers are reset to their initial detunings. The cooled atoms can propagate freely before a new cooling cycle starts. Directly in front of the collimating aperture of the atomic beam an electronically driven mechanical shutter with a rise time $t = 500$ μs allows us to unblock the atomic beam in phase with the slowing light pulse. As a consequence the arrival of fast thermal atoms simultaneously with the slowed atoms at the detection zone is strongly suppressed.

With this atomic beam source it is possible to generate pulses of slow cesium atoms spatially extending over a length of about 30 cm. The final longitudinal atomic velocity v can be chosen between 0 and 200 m/s with a relative uncertainty of 5 m/s. The longitudinal velocity spread was determined by Doppler-free spectroscopy to be smaller than 3 m/s. In total we achieve a flux of 10^7 slow atoms per pulse, i.e., 10^8 atoms/s. From fluorescence spectra taken in an inhomogeneous magnetic field we calculate that more than 93% of these atoms are in the $F = 4$, $m_F = 4$ magnetic substate. Atoms in other magnetic substates can thus be neglected in the following experiments. Approximately 8×10^4 spontaneous absorption-emission processes per atom during the slowing lead to a transverse heating of the atomic beam. Due to the high mass transverse diffusion of cesium atoms out of the slowing laser is not significant [18]. The transverse beam profile becomes a Gaussian with a full width at half maximum of typically 8 mm (11 mm) for a final velocity of 90 m/s (35 m/s).

C. Recording of atomic beam profiles

At variable distances behind the magnetic components the atoms traverse a detection zone. Resonant laser light from a diode laser locked to the $F = 4 \rightarrow 5$ line of the cesium D_2 transition is weakly focused into the vacuum chamber with a cylindrical lens, forming a light sheet with a focal line waist of 110 μm and a Rayleigh zone length of 6 mm.

During their passage through the light sheet the atoms fluoresce, and the spatial distribution of the fluorescence light that corresponds to the density distribution of the atomic beam is recorded with an image-intensified slow scan charge-coupled device (CCD) camera. The image intensifier can be gated for times as short as 100 ns allowing time-resolved detection. The 12-bit gray-scale video image is available on a computer for quantitative analysis. Formerly only a standard technique in combustion research, this method was first used in atomic beam monitoring by Esslinger, Hemmerich, and Hänsch [19].

Since 2.5 video images per second can be taken, real-time alignment of the light sheet and atomic beam with the assistance of standard vacuum manipulators is possible. The CCD camera was calibrated absolutely and its linearity was tested. A photon flux of about 25 (photons/s)/pixel is sufficient to overcome the noise level. With our maximum 1:1.4 imaging ratio for our camera optics we achieve a spatial resolution of 160 μm with the dominant contribution coming from the image intensifier, which spreads a signal over 5×5 pixels (each pixel is 23×23 μm^2 wide).

In order not to obstruct the light path of the slowing lasers, the CCD camera was mounted slightly off the optical axis. Therefore all video images exhibit a small parallax.

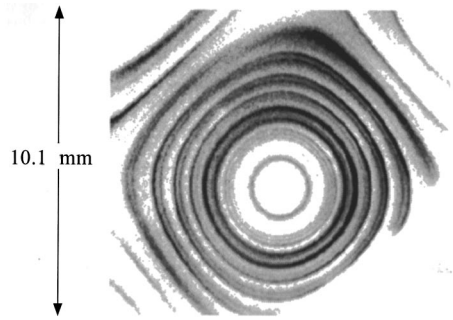

FIG. 4. Fluorescence distribution of a thermal cesium beam in a magnetic quadrupole field. The laser frequency of the detection laser is detuned by -850 MHz with respect to the zero field $F=4\rightarrow5$ transition. Different atomic transitions are magnetically shifted into resonance and each produces a ring of fluorescence light. Position and shape of the rings correspond to contour lines of the magnetic field strength. Dark color means high fluorescence intensity.

IV. THE MAGNETIC QUADRUPOLE RING

We have used magnetic quadrupole rings with a length of 38.1 mm and an open bore of 22 mm, consisting of 16 segments each (Fig. 1 and Table I). They were made from $SmCo_5$ with remanence $B_r=0.95$ T and possess a magnetic flux density gradient of 0.87 T/cm [20]. Theoretically the next higher multipole for these quadrupoles is, according to Eq. (8), the 36-pole. Due to imperfect segments and geometry, however, small contaminations enter at the hexapole and octupole level already.

A. Magnetic contour mapping

An atomic beam is a sensitive probe of the field distribution because resonance frequencies strongly depend on the local magnetic field strength. A 10-MHz Zeeman shift, i.e., more than a typical linewidth for transverse Doppler free excitation of an atomic beam, is caused by no more than 1-mT modification of the magnetic flux density. In strong permanent multipoles such variations may occur on a scale of a few 10 μm. Hence a recording of the fluorescence of the atomic beam near or even inside the magnetic multipoles gives a contour plot of the corresponding magnetic field.

The video image in Fig. 4 was taken when the detection zone was placed in a 10-mm gap between two quadrupole rings situated on the atomic beam axis. The atomic beam was scanned across the ring aperture and the corresponding video images were composed into a single picture on the computer. In the inner region of the quadrupole the radially symmetric magnetic shift of the spectral lines leads to resonance rings around the magnetic axis. These rings represent the equipotential lines of the quadrupole magnet. In the outer regions the magnetic field strength decreases again and there are already contour lines observable that are not closing. Visual inspection of the contour plot shows that the deviations from the ideal quadrupole potential are negligible for about $0.5\rho_1$ of the quadrupole rings employed. In the outer region of the quadrupole higher-order multipole contributions to the magnetic field can be seen in the video image in Fig. 4 too.

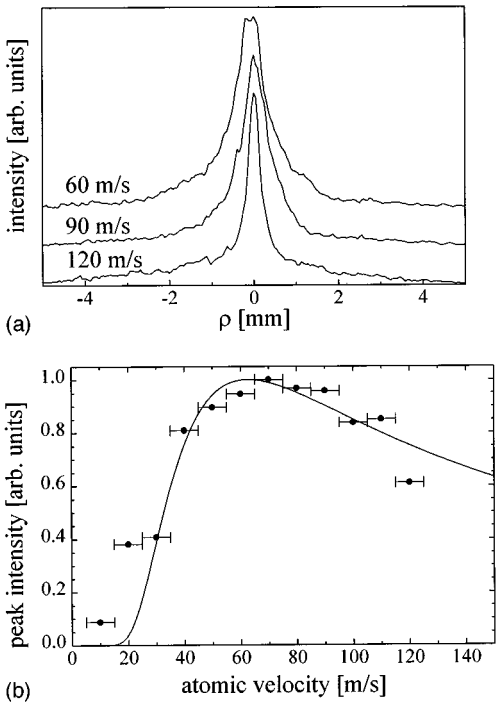

FIG. 5. Atomic beam transformation by a magnetic quadrupole ring: (a) Measured transverse fluorescence intensity distribution for different longitudinal atomic velocities. Each of the curves is normalized to the same height in order to allow a comparison of the beam shape. (b) Maximum atomic density at a fixed distance behind the magnetic quadrupole ring as a function of longitudinal atomic velocity, where the peak height at $v=70$ m/s is normalized to unity. Dots represent experimental values, the solid line is a model calculation.

B. Quadrupole prisms

When polarized atoms traverse a short magnetic quadrupole ring they experience a deflecting force that is independent of the impact radius, and the transverse velocity change is a function of the transit time only. Therefore the quadrupole ring acts analogously to a dispersing prism, or more precisely a conical prism called axicon in light optics. They were first described by McLeod who was fascinated by the extended focal line produced by axicons [21]. He suggested to use the axicon in particular for alignment procedures, but the application became obsolete when the laser was invented. Renewed interest arose when it became clear that axicons transform coherent plane waves into so-called diffraction-free Bessel beams [22].

For an experimental investigation of the atom-optical properties of an axicon a quadrupole ring was placed 15 cm behind the end of the laser slowing section. Fluorescence of the transmitted atoms was monitored by the laser light sheet at various distances behind the quadrupole ring. For a thermal atomic beam we find a circularly symmetric pattern with a sharp axial intensity maximum for a large range of distances from the quadrupole ring, corresponding to the long focal line of the light-optical axicon. Alternatively, the detection distance was kept fixed and the atomic velocity of an incident laser-cooled atomic beam was varied. Figure 5(a) shows one-dimensional profiles across the center of the transverse atomic density distribution, obtained for different

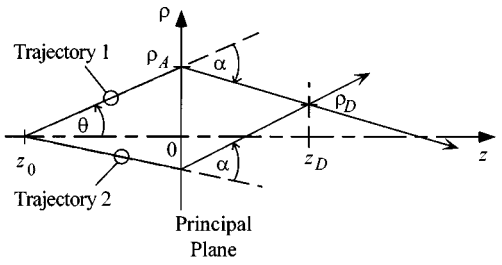

FIG. 6. The two types of atomic trajectories through a thin magnetic quadrupole ring placed at $z=0$ that connect a point z_0 on the axis with a second point at (ρ_D, z_D). Trajectory 2 crosses the optical axis before reaching point (ρ_D, z_D) whereas trajectory 1 does not.

velocities of the incident atomic beam. Each of the profiles is independently normalized to unity to allow a comparison of the beam shapes.

For a wide range of velocities the peak height of the transverse beam profiles remains fairly constant [Fig. 5(b), where the height at $v=70$ m/s is normalized to unity]. This is the analog of the extended focal line of the axicon when the fact is taken into account that faster atoms scatter fewer photons in the detection zone.

For small deflection angles $\alpha<10°$ one can describe the action of the magnetic quadrupole on an atom in a ''thin quadrupole'' model, i.e., by an instantaneous transfer of transverse momentum in the center of the quadrupole (at $z=0$). We model the cold atomic beam by a point source at z_0 (Fig. 6) with a Gaussian distribution of transverse velocity components

$$j(v_\perp)v_\perp dv_\perp d\varphi = 1/(2\pi\sigma^2)\exp(-v_\perp^2/2\sigma^2)v_\perp dv_\perp d\varphi \tag{12}$$

and a fixed longitudinal velocity v. For our Cs beam, $\sigma \approx 0.85$ m/s.

Each atom is deflected towards the axis by an angle

$$\alpha = \frac{\mu_B \beta L}{mv^2} = \frac{138}{v^2}\left(\frac{\mathrm{m}^2}{\mathrm{s}^2}\right), \tag{13}$$

independently of its incident angle and point of impact onto the aperture of the quadrupole ring. An atom starting at z_0 with angle Θ $(\Theta = v_\perp/v)$ crosses the detection zone $(z=z_D)$ at radius ρ_D (Fig. 6). Two cases have to be considered. For $\Theta > \alpha z_D/(z_D-z_0)$ atoms from a ring with radius $\rho_A = -z_0\Theta$ in the aperture are compressed into a ring of radius $\rho_D = \Theta(z_D-z_0)-\alpha z$ in the detection zone (trajectory 1 in Fig. 6). With $v_\perp = v(\alpha z_D+\rho_D)/(z_D-z_0)$ the angular distribution of the source can be transformed into a density distribution at the detection zone:

$$j_1(\rho_D)\rho_D d\rho_D d\varphi = \frac{a^2}{\pi}\frac{\alpha z_D+\rho_D}{\rho_D} \times \exp[-a^2(\alpha z_D+\rho_D)^2]\rho_D d\rho_D d\varphi, \tag{14}$$

where $a^2 = [v/\sigma(z_D-z_0)]^2/2$.

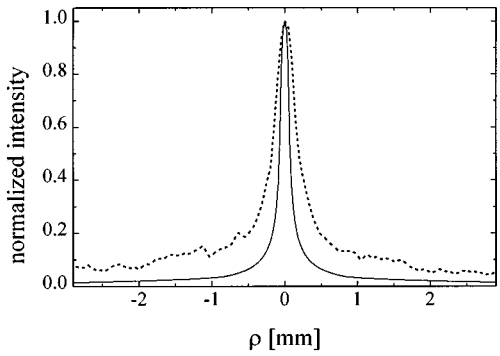

FIG. 7. Comparison of calculated (solid line) and measured (dots) transverse intensity distribution behind the magnetic quadrupole ring for a longitudinal atomic velocity of 120 m/s.

Similarly, for $\Theta < \alpha z_D/(z_D-z_0)$ atoms from a ring with radius $\rho_A = -z_0\Theta$ in the aperture are transformed into a ring of radius $\rho_D = -\Theta(z_D-z_0)+\alpha z$, giving a second contribution to the flux density (trajectory 2 in Fig. 6):

$$j_2(\rho_D)\rho_D d\rho_D d\varphi = \frac{a^2}{\pi}\frac{\alpha z_D-\rho_D}{\rho_D}\exp[-a^2(\alpha z_D-\rho_D)^2] \times \rho_D d\rho_D d\varphi. \tag{15}$$

The total flux density can then be written as

$$j(\rho_D)\rho_D d\rho_D d\varphi = [j_1(\rho_D)+j_2(\rho_D)\max(0,\alpha z_D-\rho_D)] \times \rho_D d\rho_D d\varphi. \tag{16}$$

This density distribution is numerically integrated over an area corresponding to the size of a camera pixel. Then the flux on 5×5 simulated ''camera pixels'' is averaged and used to derive a transverse density profile of the atomic beam transmitted through the magnetic quadrupole ring.

The solid line in Fig. 5(b) gives the calculated atomic flux on the axis for different longitudinal velocities. The calculated values were divided by v to account for the characteristics of the detecton process in the light sheet where the total fluorescence intensity for an atom is inversely proportional to its velocity. In the experiment, $z_D=4$ cm was fixed, and only z_0 remains as a fit parameter. For $z_0=-13$ cm the best fit between theory and experiment was achieved, which is in agreement with our experimental situation.

Although the variation of the peak intensities is well reproduced by our simple model the individual calculated profiles are too narrow (Fig. 7). In order to fully reproduce the transverse beam profiles one would have to model the exact characteristics of a chirp-slowed atomic beam. This is very difficult because in reality at the end of the slowing cycle cold atoms are spread out over about 30 cm in space along the beam axis. Furthermore, the angular divergence σ of the atomic distribution depends on the position along this spatial pulse of atoms. Finally, for larger final velocities the slowing stops earlier, and the cold atoms start farther away from the quadrupole ring. However, no deeper insight into the behavior of a magnetic quadrupole ring as an atom-optical component can be gained from such a ''full-blown'' treatment of the beam source characteristics.

It should be noted that for a narrow atomic beam incident at a large radius the magnetic axicon approaches the limit of a plane prism, which, from light optics, is known to deflect beams and also to be dispersive.

V. HEXAPOLE LENSES

In a magnetic hexapole ring the force on a paramagnetic low-field-seeking atom in a Zeeman substate with maximum m_F value is linearly increasing with radial coordinate ρ, which leads to harmonic binding to the magnetic axis:

$$F = -\delta\mu_B(\partial^2|B|/\partial\rho^2)\rho, \tag{17}$$

with $\delta = 1$ for an alkali atom. This was first realized by Paul and Friedburg and was used to focus and polarize thermal atomic beams [1]. We have taken the focal length of such magnetic lenses from the meter to the more convenient centimeter domain by using strong permanent magnets for field generation and low velocity atomic beams with small velocity spread for reduced chromaticity.

During the experiments described here we have used two different hexapole magnets (called type I and II). Both were made from 12 Nd-Fe-B segments with a magnetic remanence $B_r = 1.12$ T (Figs. 1 and 2 and Table I).

In a systematic investigation we have varied the magnetic focal length as a function of atomic beam velocity. From Eq. (17) one derives a ''thin lens'' approximation for the focal length:

$$f = \frac{mv^2/2}{\mu_B(\partial^2 B/\partial\rho^2)L}. \tag{18}$$

For the determination of the focal length we have monitored the atomic beam profile at a preset distance from the type I hexapole lens. The final beam velocity was then tuned until minimum spatial extension of the beam, i.e., the circle of least confusion, was reached. Results are given in Fig. 8(a) showing good agreement with the thin lens approximation over a wide range of focal lengths and even close to the magnetic component.

We have also studied the width of the focal spot as a function of atomic velocity, i.e., as a function of focal length f [Fig. 8(b)]. With decreasing focal length the spot size decreases. This is to be expected from geometrical optics for the imaging of a flat object. It reaches a minimum of 325 μm diameter at $f = 2.65$ cm, corresponding to $v = 36$ m/s. The resolution of our detection scheme during these experiments was 210 μm (290 μm for $f > 11.75$ cm) because of geometrical restrictions in our setup and is indicated in Fig. 8(b).

For the 11-mm cross-section incident beam the observed spot size means a more than 1000-fold increase in flux density. The brightness of a laser-cooled atomic beam,

$$\text{brightness} = \frac{\text{atomic flux}}{(\text{unit area}) \times (\text{divergence}) \times (\text{velocity interval})}, \tag{19}$$

may be further enhanced by transverse cooling at the focal spot. A detailed investigation of the limitations of the focal spot size has not yet been carried out. It is the subject of further research exploring the influence of geometric and chromatic aberrations. The diffraction limit, which is of order $\lambda_{\text{atom}} f/D \approx 1$ nm, may remain elusive, but a submicrometer focusing device would already make an interesting stylus for writing lateral structures, especially when combined with a high atomic flux.

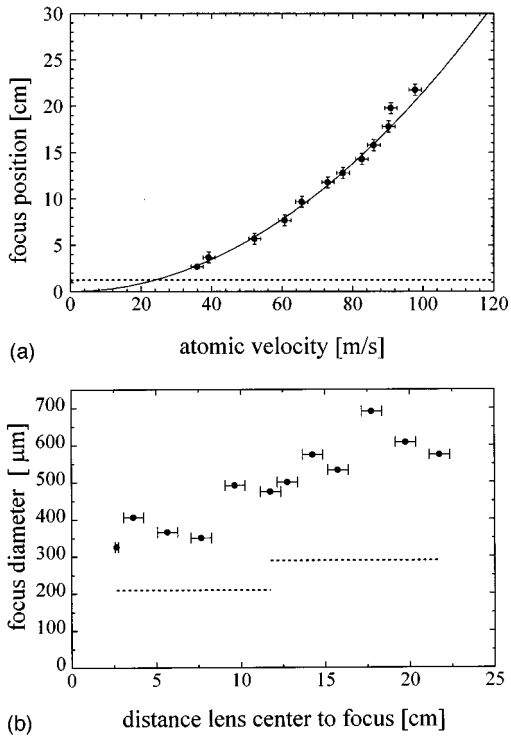

FIG. 8. Experimental results of the atomic beam focusing experiments with a magnetic hexapole lens of type I (cf. Table I): (a) Focus position behind the hexapole lens as a function of atomic velocity v. The data points (dots) are compared with a calculation of focus position based on the thin lens approximation (solid line). The dotted horizontal line indicates the axial extension of the magnetic lens. (b) Experimental data showing the focus diameter (full width at half maximum) as a function of focus position. The smallest spot size of 325 μm was obtained with a beam of 11 mm diameter for a velocity $v = 36$ m/s. The dotted horizontal lines indicate the spatial resolution of the detection system.

A. Imaging

To demonstrate the imaging capabilities of our magnetic hexapole ring a setup analogous to a light-optical slide projector has been constructed (Fig. 9). A slab of PMMA (polymethylmethacrylate) with a pattern of holes placed into the atomic beam path served as the slide. The resulting spatial atomic distribution was then imaged by a magnetic lens. Imaging distances $g = 98$ mm and $b = 120$ mm were kept fixed while the focal length was varied by tuning the final atomic velocity. For an atomic velocity $v = 110$ m/s a focus is produced in the detection zone. With lower and lower atomic velocity an inverted real image evolves. At $v = 70$ m/s a sharp image with a magnification of 1.4 is obtained. Reducing the atomic velocity further blurs the image again (Fig. 10). A second imaging distance $b = 80$ mm leads to a demagnified (0.8) image [23].

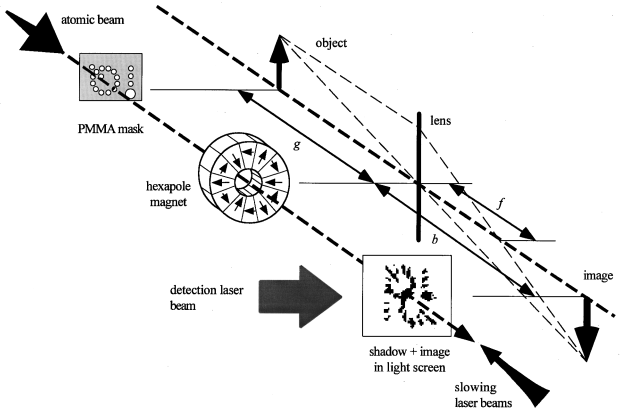

FIG. 9. Experimental setup for the imaging experiment (left-hand side) shown in analogy to the projection of an optical slide (right-hand side).

An essential criterion for the application of any imaging system is its resolving power. The ultimate diffraction limit of order 1 nm for a typical magnetic atom optical lens is increased by multiple deficiencies. The magnetic components lack complete rotational symmetry around the z axis. Therefore there are more than the usual five third-order aberrations (Gauß-Seidel aberrations) [24] well known from light optics. Of these aberrations the spherical aberration is most important for focusing experiments but the lens shows an excellently harmonic potential (Fig. 2), so that this is currently a minor problem.

Longitudinal velocity spread leads to chromatic aberrations while transverse velocity spread increases the focal spot size. Both velocity spreads can be reduced by further optical cooling [25,26].

In addition, errors linked to the atomic beam preparation occur that have no analogy in other branches of particle optics. Imperfect polarization of the atomic beam leads to different deflection angles depending on the Zeeman sublevel the atoms are in but can be overcome by a more sophisticated optical beam preparation [27]. Furthermore an asymmetric imaging error due to the mass of the atoms moving in the Earth's gravitational field has to be accounted for. Therefore imaging should be as compact as possible.

B. An atom optical telescope

Preparation of a slow atomic beam requires an axial counterpropagating slowing laser beam. For actual applications it

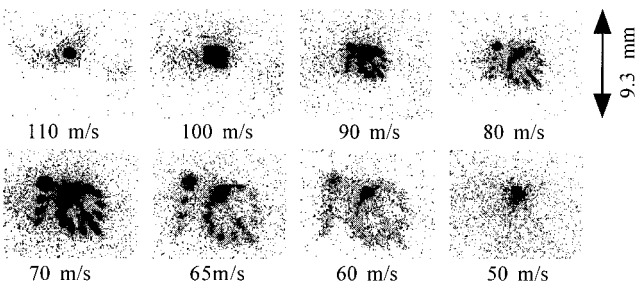

FIG. 10. Atomic fluorescence intensity distribution for a fixed imaging distance of $b=120$ mm as a function of atomic velocity v (dark color means high atomic density). These images were taken with the setup shown in Fig. 9.

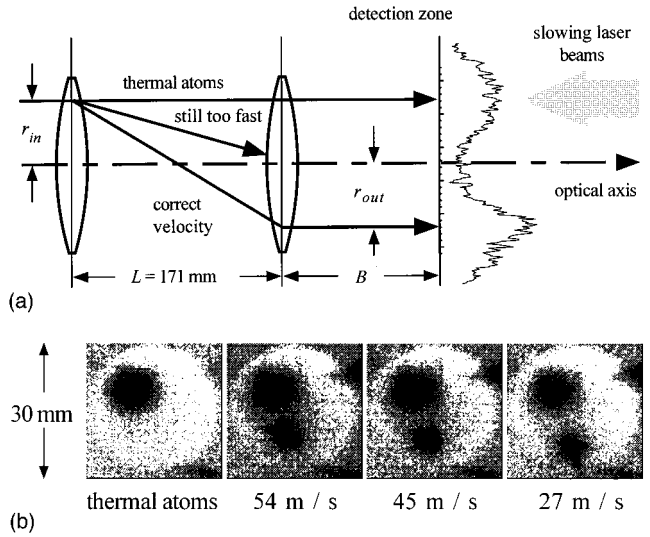

FIG. 11. (a) Schematic drawing of an atom optical telescope. The telescope is built from two identical magnetic hexapole lenses of type II (cf. Table I). A line profile of the intensity in one of the video images [(b), $v=27$ m/s] is added at the right-hand side. (b) Spatial distribution of atomic fluorescence after the atoms have passed through the atom optical telescope as a function of atomic velocity v. The detection time window is slightly shifted in these experiments so that the thermal atomic beam is visible in the video frame for positional reference (dark color means high atomic density).

is desirable to separate the axis of the newly prepared and the remaining thermal beam. For this purpose we have assembled a telescope as a classic application of lenses, which is operated off axis in order to displace the slowed atoms. A demonstration of such a telescope is still an ambitious task since beam divergence and dispersion rapidly increase at the low atomic velocities required. We have used two identical magnetic lenses of type II separated by a distance $L=171$ mm. The laser and the atomic beam path have been adjusted parallel to the magnetic axis but with a displacement of $r_{\mathrm{in}}=5$ mm [Fig. 11(a)]. Due to the magnetic lenses the atoms experience a velocity-dependent deflection towards the optical axis which begins to be noticeable for velocities less than $v=100$ m/s.

When the atomic velocity is further reduced the cooled atoms are deflected from the path of the thermal atoms [Fig. 11(b)]. Near $v=35$ m/s the center of the second lens is crossed and for even smaller v the direction of the beam of cold atoms is reoriented towards the magnetic axis. In Fig. 12 we observe a corresponding flattening of the displacement $r_{\mathrm{in}}+r_{\mathrm{out}}$ of the slow beam with respect to the thermal beam when the velocity approaches the predicted telescope velocity $v=27$ m/s. For this velocity the focal length of each lens corresponds to $L/2$, and the telescopic case is reached. The spatial separation of the two centers amounts to 10 mm and is limited by the inner diameter of our magnetic lenses. Figure 12 also shows a comparison with a simple calculation based on the $ABCD$-matrix formalism, which shows good agreement for velocities $v>35$ m/s.

VI. CONCLUSIONS

Formerly the chromaticity and the relatively weak forces of magnetic components on fast atoms have made their use

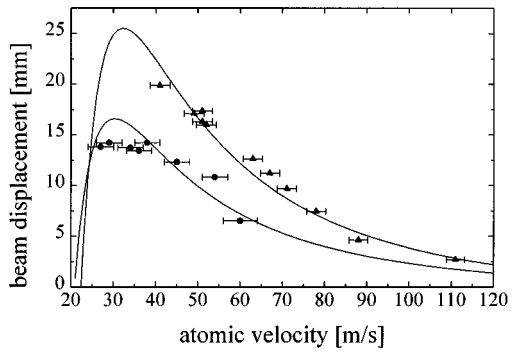

FIG. 12. Comparison of experimental data extracted from line profiles of video images [cf. Fig. 11(b)] and a calculation based on an *ABCD*-matrix formalism (solid lines) for the spatial separation of cold and thermal atoms. Triangles and circles represent different positions B of the light sheet detection after the atoms passed the telescope (circles, $B=130$ mm; triangles, $B=200$ mm). For $v=27$ m/s the situation of a confocal telescope is reached.

cumbersome for many atom-optical applications. Readily available optical cooling techniques and steeper magnetic gradients of permanent magnets now offer new possibilities to control neutral atom motion. With a chirp-slowed cesium atomic beam and two-dimensional recording of atomic beam profiles we have demonstrated the following: magnetic quadrupole rings acting as conical prisms or axicons for atom optics; magnetic hexapole lenses with focal lengths in the cm region and minimum spot size of less than 325 μm corresponding to a more than 1000-fold increase of atomic flux density; magnetic magnification and demagnification of a nontrivial object illuminated with velocity-narrowed slow atomic beams; a magnetic telescope, which is useful to separate fast thermal and slowed atoms by exploiting velocity dispersion.

In order to explore the ultimate limits of our magnetic atom-optical components a better defined beam source than a chirp-slowed atomic beam is necessary. Such a source might be provided by a Zeeman slower [18] or atoms dropped from a magneto-optical trap [11].

ACKNOWLEDGMENTS

We thank V. Frerichs for support with the mathematical description of the permanent magnets. The relationship between magnetic quadrupoles and light optical axicons was pointed out to us by K. M. Knaak (Universität Heidelberg) and S. Herminghaus (Universität Konstanz). We also thank A. Hardt and S. Martin (Forschungszentrum Jülich GmbH) for providing the magnetic quadrupole rings. This work was supported by the Deutsche Forschungsgemeinschaft.

[1] H. Friedburg and W. Paul, Naturwissenschaft. **38**, 159 (1951); H. Friedburg, Z. Phys. **130**, 493 (1951); H. G. Bennewitz and W. Paul, *ibid.* **139**, 489 (1954).
[2] O. Stern, Z. Phys. **7**, 249 (1921).
[3] I. I. Rabi, S. Millman, P. Kusch, and J. Zacharias, Phys. Rev. **55**, 526 (1939).
[4] C. S. Adams, Contemp. Phys. **35**, 1 (1994); C. S. Adams, M. Sigel, and J. Mlynek, Phys. Rep. **240**, 143 (1994).
[5] D. M. Giltner, R. W. McGowan, and S. A. Lee, Phys. Rev. Lett. **75**, 2638 (1995).
[6] E. M. Rasel, M. K. Oberthaler, H. Batelaan, J. Schmiedmayer, and A. Zeilinger, Phys. Rev. Lett. **75**, 2633 (1995).
[7] J. Vanier and C. Audoin, *The Quantum Physics of Atomic Frequency Standards* (Hilger, Bristol, 1989).
[8] H. Metcalf, W. Philips, and J. Prodan, Bull. Am. Phys. Soc. **29**, 785 (1984).
[9] A. I. Sidorov, R. J. McLean, W. J. Rowlands, D. C. Lau, J. E. Murphy, M. Walkiewicz, G. I. Opat, and P. Hannaford, Quantum Semiclass Opt. **8**, 713 (1996).
[10] C. Szymanowski, Diploma thesis, University of Hannover, Germany, 1995 (unpublished); C. Szymanowski, F. Lison, D. Haubrich, A. Goepfert, R. Wynands, and D. Meschede, Verhandl. DPG (VI) **31**, 260 (1996).
[11] T. M. Roach, H. Abele, M. G. Boshier, H. L. Grossman, K. P. Zetie, and E. A. Hinds, Phys. Rev. Lett. **75**, 629 (1995).
[12] K. Halbach, Nucl. Instrum. Methods **169**, 1 (1980); **187**, 109 (1981); Int. J. Mod. Phys. B **4**, 1201 (1990).
[13] W. G. Kaenders, V. Frerichs, F. Schröder, and D. Meschede, Hyperfine Interact. **76**, 221 (1993).
[14] *Proceedings of CERN Accelerator School: Magnetic Measurement and Alignment*, edited by S. Turner (CERN, Geneva, 1992).
[15] H. Zijlstra, *Experimental Methods in Magnetism, 2. Measurement of Magnetic Quantities* (North-Holland, Amsterdam, 1967).
[16] For example, R. N. Watts and C. E. Wieman, Opt. Lett. **11**, 291 (1986).
[17] W. Ertmer, R. Blatt, J. L. Hall, and M. Zhu, Phys. Rev. Lett. **54**, 996 (1985).
[18] M. A. Joffe, W. Ketterle, A. Martin, and D. E. Pritchard, J. Opt. Soc. Am. B **12**, 2257 (1992).
[19] T. Esslinger, A. Hemmerich, and T. W. Hänsch, Opt. Commun. **93**, 49 (1992).
[20] R. F. Holsinger and K. Halbach (unpublished).
[21] J. H. McLeod, J. Opt. Soc. Am. **44**, 592 (1954); **50**, 166 (1960).
[22] J. Durnin, J. J. Miceli, Jr., and J. H. Eberly, Phys. Rev. Lett. **58**, 1499 (1987); J. Durnin, J. Opt. Soc. Am. A **4**, 651 (1987).
[23] W. G. Kaenders, F. Lison, A. Richter, R. Wynands, and D. Meschede, Nature **375**, 214 (1995).
[24] M. Born and E. Wolf, *Principles of Optics*, 6th ed. (Pergamon, Oxford, 1980).
[25] J. Nellessen, J. Werner, and W. Ertmer, Opt. Commun. **78**, 300 (1990).
[26] R. Riis, D. S. Weiss, K. A. Moler, and S. Chu, Phys. Rev. Lett. **64**, 1658 (1990).
[27] B. P. Masterson, C. Tanner, H. Patrick, and C. E. Wieman, Phys. Rev. A **47**, 2139 (1993).